

# Deep Feature-specific Imaging

YIZHOU LU<sup>1</sup> AND ANDREAS VELTEN<sup>2,1,\*</sup>

<sup>1</sup>*Department of Electrical and Computer Engineering, University of Wisconsin-Madison, Engineering Hall, 2415, 1415 Engineering Dr, Madison, WI 53706, USA*

<sup>2</sup>*Department of Biostatistics and Medical Informatics, University of Wisconsin-Madison, Warf Office Bldg, 610 Walnut St Room 201, Madison, WI 53726, USA*

\**velten@wisc.edu*

## Abstract:

Modern photon-counting sensors are increasingly dominated by Poisson noise, yet conventional Feature-Specific Imaging (FSI) is optimized for additive Gaussian noise, leading to suboptimal performance and a loss of its advantages under Poisson noise. To address this, we introduce DeepFSI, a novel end-to-end optical-electronic framework. DeepFSI "unfreezes" traditional FSI masks, enabling a deep neural network to learn globally optimal measurement masks by computing gradients directly under realistic Poisson and additive noise conditions. Our simulations and experiments demonstrate DeepFSI's superior feature fidelity and task performance compared to conventional FSI with predefined masks, especially in Poisson-Noise-dominant environments. DeepFSI also exhibits enhanced robustness to design choices and performs well under additive Gaussian noise, representing a significant advance for noise-robust computational imaging in photon-limited applications.

## 1. Introduction

The development of advanced sensor technologies, particularly photon-counting sensors (PCS) like Single-Photon Avalanche Diodes (SPADs), has introduced unprecedented temporal precision for photon-limited applications [1–4]. PCS have been increasingly explored in computational imaging (CI) frameworks to enhance performance. CI uses optical coding followed by computational decoding [5] and the coding is traditionally designed for additive Gaussian noise (AGN). Generally, it can be expressed by

$$\mathbf{y} = \mathbf{M}\mathbf{x}, \quad (1)$$

where  $\mathbf{y}$  incorporates the measured photon numbers at sensor,  $\mathbf{M}$  is the sensing matrix of a given coding design, and  $\mathbf{x}$  is the vector representation of an image [5–7]. Due to the no read-noise on PCS, signal-dependent Poisson noise (PN) dominates in most imaging scenarios, undermining the performance gains typically achieved by such traditional CI methods [5]. To overcome this challenge, Cossairt et al. proposed task-specific imaging, often exemplified by feature-specific imaging [8], as a promising direction for future research [5].

Feature-specific Imaging (FSI) utilizes prior knowledge about the scene and task, for example in the form of principal components obtained via principal component analysis (PCA) that are applied to the image before the light is measured and digitized. Using these coding patterns, it is possible to extract features of interest before digitization, application of Poisson noise, and digital processing. FSI offers benefits in reducing data burden, improving efficiency, and enhancing feature fidelity in high-AGN environments [9]. However, conventional FSI paradigms, including Neifeld et al.'s foundational work and subsequent developments, are primarily designed and optimized under AGN [8–11]. Its performance degrades in conditions where PN becomes the primary noise source, making it suboptimal in such cases [9]. Indeed, early investigations into FSI have explicitly shown that its multiplexing advantages from coding disappear when moving from AGN to PN, resulting in no feature-fidelity improvement over conventional, non-computational imaging methods [8]. Therefore, it is essential to develop new feature extraction and measurement optimization methods for FSI that are intrinsically robust to PN, moving beyond ad-hoc noise

handling at the post-processing stage. Specifically, for PCS, designing PN-aware algorithms for the entire FSI pipeline is becoming imperative.

In this context, we propose a Deep Feature-specific Imaging (DeepFSI) model to address this challenge. DeepFSI is an end-to-end model incorporating an optical-coding layer on hardware end with a deep-neural-network model on software end for specific computer vision tasks. During the training stage, DeepFSI simulates AGN and PN after the optical-coding layer, and computes the gradients under the noise by to optimize the coding for optimal feature extraction performance via backpropagation. Unlike conventional FSI, which relies on predefined and fixed coding patterns, DeepFSI enables dynamic, data-driven coding optimized for task-specific features. Following the setup in [10], we use a single-pixel camera (SPC) as the primary testbed for both simulations and experiments. The methodology developed on an SPC should be generalized to any coding-based vision systems. Our results show that DeepFSI outperforms conventional FSI under PN. Furthermore, unlike conventional FSI methods requiring an accurate estimate of the number of features and careful noise level estimation to avoid improper compression, DeepFSI demonstrates much greater robustness to inaccuracies in feature count. This stability not only minimizes performance degradation under mismatched conditions, but also broadens the applicability of DeepFSI beyond its specific training scenarios, enhancing its usefulness and impact in real-world applications.

The main contributions of the proposed DeepFSI model are listed below.

1. Bridging the gap between traditional FSI and Poisson noise by incorporating noise generation into model training.
2. Exceeding the limitation arising from using unsupervised methods, such as PCA, in supervised classification tasks.
3. Enhancing the robustness and performance with suboptimal assumption in application, such as varying noise level and number of masks, suggesting broader utility.
4. Showing that AGN-favored coding is suboptimal under PN conditions.

## 2. Related Work

The studies most relevant to our research are summarized below.

- **Evolution in FSI.** FSI is a paradigm that directly measures features of interest rather than a full image using prior knowledge such as PCA for efficiency and feature fidelity [8]. It can be viewed as a variant of compressed sensing [10] and a specific form of task-specific imaging [8]. Moreover, FSI can be adopted in vision systems for direct classification tasks skipping the reconstruction step [11]. Using an SPC is a concise and straightforward way to develop FSI algorithms, which can be seamlessly generalized to systems with other coding-based frameworks. Conventional FSI is designed for AGN [8–11], and promoting it to systems mainly affected by PN remains an issue to be resolved [10].
- **Noise-dependent Coding Optimization.** Conventional works in CI area have assumed AGN as the primary noise source and recognized Hadamard as the best coding design [5, 7, 12]. It is recognized that coding optimal for AGN is suboptimal for PN in many different CI applications [5–7, 12, 13]. Harwit et al. [7] proved the optimality of Hadamard coding under signal-independent noise, but opposed using it under PN. Raginsky et al. [6] have proved the upper bound of the reconstruction error in compressed sensing behaves differently when transiting from AGN to PN. Cossairt et al. [5] and Mitra et al. [13] have demonstrated that AGN-optimal coding designs cannot give rise to ideal performance gain when PN is predominant. Mitra et al. [13] further proposed that data-driven coding

designs using data priors outperform classical ones such as Hadamard. Wuttig and Ratner, et al. [12, 14] introduced Poisson-noise-aware optimization techniques for coding matrices that outperform Hadamard in the presence of moderate signal-dependent noise. However, their analysis neglects the data priors, leading to suboptimal matrices for greater Poisson noise [13]. Additionally, attempts at matrix optimization focusing on minimal mutual coherence [15] do not adequately consider Poisson noise, as highlighted in this study.

- **End-to-end Optimization and Learned Optics.** This method jointly optimizes optical coding design and digital signal processing to achieve optimal overall performance [16–19]. In previous works, this idea was usually implemented without considering Poisson noise in cost functions [18, 20–27] or without optimizing masks with gradient incorporating Poisson distribution [16, 27–31]. Chang et al. [20] proposed a hybrid optical-electronic model demonstrating learning optical elements. Their primary goal is computational efficiency, and their system is not designed for Poisson noise. Wang et al. [30] successfully implemented a neural network model for handwritten number classification on an optical device with limited photon budget, demonstrating the potential for AI-assisted optimization of coding schemes. However, Poisson noise was considered only in model testing where the most robust model was picked among a set of different initialization seeds [30]. Xu et al. [31] examined the robustness of the proposed neural network model to Poisson noise, but their training process does not explicitly incorporate the gradients affected by Poisson noise. Tseng et al. [32] proposed a noise-aware optimization methodology, but their work focuses on the point-spread function on camera design. Mitra et al. [13] used a Gaussian Mixture Model and priors from training data to optimize coding, but this work focuses on image reconstruction. While prior works have explored end-to-end learning for various imaging tasks and some have addressed noise during inference, none have specifically extended FSI paradigm to jointly optimize the optical sensing matrix and feature extraction network explicitly for the challenging Poisson noise regime. Our work on DeepFSI directly addresses this critical gap arising from the insufficient understanding of Poisson noise and enhances the practicality of FSI techniques.

### 3. Background

#### 3.1. Single-pixel Camera

The single-pixel camera (SPC) shown in Fig. 1 is a popular example that demonstrates and tests the effect of a given coding design. Coding optimization focuses on the spatial dimensions, but the methodology obtained from it can be generalized to other coding-based vision systems. Our SPC uses a photon multiplier tube (PMT), a rapid single-pixel detector using photon-counting technology, in conjunction with a digital micromirror device (DMD) to sequentially project a sensing matrix  $\mathbf{M}$  by modulating various patterns on the DMD [13]. Its measurement process mathematically follows the Eq. 1. Here,  $\mathbf{x} \in \mathbb{R}^{N \times 1}$  is the image representation of the field of view (FOV), which consists of  $N$  pixels, and is measured by linear projections or masks,  $\mathbf{M} \in \mathbb{R}^{m \times N}$  to attain corresponding flux levels or photon counts,  $\mathbf{y} \in \mathbb{R}^{m \times 1}$  [6]. Physically,  $\mathbf{M}$  is the optical coding, and can be implemented on the DMD by directing or blocking different parts of the incoming light from  $\mathbf{x}$  [33] and averaging them on sensors that digitize the detected flux levels, or photon counts,  $\mathbf{y}$ . The patterns used for this objective are called masks, corresponding to the rows of  $\mathbf{M}$ . If the sensing matrix  $\mathbf{M}$  is full-rank,  $\mathbf{x}$  can be reconstructed by  $\mathbf{M}^{-1}\mathbf{y}$ . However, even when  $m < N$ , we can still recover  $\mathbf{x}$  via compressed sensing. Although Hadamard matrices are considered effective in coding, their suitability diminishes in the presence of data-dependent Poisson noise [7, 13]. In the FSI narrative, coding can also be interpreted as feature extraction, where  $\mathbf{y}$  can be used directly in classification tasks as a feature vector. In this case, the following recovery of  $\mathbf{x}$  in Fig. 1 is not necessary.

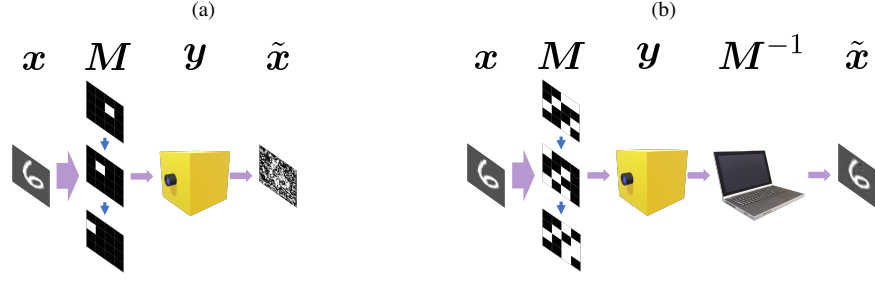


Fig. 1. Single-pixel camera configuration.  $x$ : field of view,  $M$ : masks of coding,  $y$ : counted photon numbers at the sensor,  $M^{-1}$ : reconstruction operator,  $\tilde{x}$ : reconstructed object. (a) Only one pixel (white) is scanned in each measurement, and the measured data requires no reconstruction. (b) The sum of all white pixels is measured in each measurement and it requires a decoding step to reconstruct the field of view.

### 3.2. Selection of Sensing Matrix

In this work, we categorize different types of  $M$  into raster scan, impulse imaging, non-FSI Codes, and FSI Codes. Raster scan (RS), demonstrated in Fig. 1a, refers to a pixel-wise scanning approach, while impulse imaging (II), the gold standard in this work, involves an ideal sensor collecting the entire data spectrum simultaneously. In this work where the object  $x$  is a 2D image, II can be interpreted as an N-pixel array and other sensing matrices remain on a single pixel. However, when  $x$  is a hyperspectral, the fabrication of impulse imaging camera can be very challenging. Since each pixel in II is exposed for the entire measurement period, it is explicit that II is the supreme among all strategies. Non-FSI and FSI codes constitute basis scan, shown in Fig. 1b. Non-FSI Codes include classic, task-independent masks such as Hadamard basis (HB) as well as truncated Hadamard (TH) codes, which preserve only the low-frequency components of the Hadamard matrix. FSI Codes are task-specific and must be derived from training data, with PCA-based FSI and the proposed DeepFSI falling into this category.

### 3.3. Model under Noise

This project investigates two noise models. The first one is AGN related to dark current or read noise from imperfect sensor materials, which mainly originates from thermal vibrations of atoms at sensors. In this noise model, Eq. 1 becomes:

$$\tilde{y} = Mx + \epsilon, \quad (2)$$

where  $\epsilon \sim \mathcal{N}(\mathbf{0}, \sigma^2 \mathbf{I})$ , and  $\sigma$  is the standard deviation. The other noise model is photon noise, which arises from the statistical nature of photons [34]. In most prior research, this is approximated as PN, and the measurement equations associated with this noise model typically follow a Poisson distribution:

$$\begin{aligned} \tilde{y} &\sim \text{Poisson}(Mx) \\ \Pr(\tilde{y}_i = k) &= \frac{y_i^k \exp(-y_i)}{k!}, \end{aligned} \quad (3)$$

where  $y_i = \sum_{j=1}^N M_{ij} x_j$  [6]. While PN is the best way to approximate photon noise at this stage, its nonlinearity adds complexities to the design and optimization of affected systems, and the use of Poisson random functions eliminates gradients, making it difficult to optimize the hardware

components in an end-to-end model. To address these shortcomings, this project focuses on the signal dependency of PN and adopts the MLGauss model that uses a Gaussian variable with mean-variance equivalence [5, 13, 35], formulated as

$$\begin{cases} \tilde{\mathbf{y}} = \mathbf{M}\mathbf{x} + \mathbf{J}, \\ \mathbf{J} = (\mathbf{M}\mathbf{x})^{\circ\frac{1}{2}} \odot \boldsymbol{\epsilon}, \\ \boldsymbol{\epsilon} \sim \mathcal{N}(0, \mathbf{I}), \end{cases} \quad (4)$$

where  $\circ\frac{1}{2}$  represents element-wise square root, and  $\odot$  stands for element-wise product. It substitutes conventional Poisson approximations whenever a gradient computation is required in training stage, yet the term "Poisson" is retained for consistency with other classical models involving no hardware optimization, facilitating straightforward comparisons. For model testing, all models employ the PN model, as gradient computation is no longer required.

### 3.4. Restrictions of Coding Designs

While we can identify the optimal sensing matrix  $\mathbf{M}$  tailored to the tasks at hand, we acknowledge that the optimization problem about  $\mathbf{M}$  may not exhibit convexity. This is attributed to the presence of two constraining factors. Consequently, achieving globally optimal masks may not be universally feasible within the scope of this problem.

1. **Flux-preserving** [6]. The SPC model involves the allocation of photons available within  $\mathbf{M}$ , as discussed in [9]. It is important to ensure that  $\mathbf{M}$  does not produce additional photons through improper entries [9]. Mathematically, for the  $i_{\text{th}}$  mask,  $\sup \sum_{i=1}^m M_{ij} = 1, \forall j \in \{1, 2, \dots, N\}$  [9].
2. **Positivity-preserving** [6]. It is not possible to physically implement negative values for masks  $\mathbf{M}$ , as demonstrated in [6, 9]. In this project, we used the dual-rail approach as outlined in the work of Neifeld et al. where positive and negative entries of a mask give rise to two separate measurements [9]. Mathematically, for the  $i_{\text{th}}$  mask,  $y_i = F(\sum_{j=1}^N \text{sgn}(M_{ij}) M_{ij}x_j) - F(-\sum_{j=1}^N \text{sgn}(-M_{ij}) M_{ij}x_j)$ , where operator  $F$  is about the noise generation explained in Section 3.3 and  $\text{sgn}$  is the step function returning 1 for positive values and 0 for negative values.

## 4. Methods

### 4.1. Model Design

Classification tasks are the proper venue to test feature fidelity of coding designs. All coding designs in this project for classification tasks share the same fundamental model structure, as illustrated in Fig. 2. In this project, we apply our model to the classification of handwritten number with the MNIST dataset. To classify handwritten numbers using optical devices with limited photon budget, we built a PyTorch-based pipeline consisting of a hardware-end *scanner* module including  $\mathbf{M}$  and a noise generator to simulate the acquisition of  $\tilde{\mathbf{y}}$  described in Eq. 2 and Eq. 3, and a software-end *classifier* module classifying the measured objects by  $\tilde{\mathbf{y}}$ . For the classification task, we utilized a two-hidden layer artificial neural network (ANN) with 40 and 128 nodes, serving as the primary model. To avoid overfitting and enhance generalizability, we applied dropout after each hidden layer, followed by a rectified linear unit (ReLU) activation layer. During model training, the scanner computes the photon counts with noise and then transmits these data to the classifier. The noise is sampled from a predefined noise distribution and varies across epochs. Once the loss has been computed, the gradient descent is used to optimize the classifier parameters. What sets DeepFSI apart from other coding designs is the learnable  $\mathbf{M}$  that is not predefined nor fixed. In other words, backpropagation is extended to the scanner,

allowing the simultaneous optimization of the scanner and the classifier under different noise models. We adopt the reparameterization trick, which is incorporated in PyTorch, to estimate the gradient affected by noise simulated by random number generator functions. This approach offers distinct advantages compared to traditional methods, which typically optimize the classifier independently of the scanner or optimize the scanner without the appropriate noise model. In our design, though the hybrid optimization fully relies on computer simulation, it is feasible to load the scanner parameters into the coding optics to build a real camera, which is also demonstrated in this work. Once operational, this model can serve various purposes, ranging from object classification and signal recovery to end-to-end camera design.

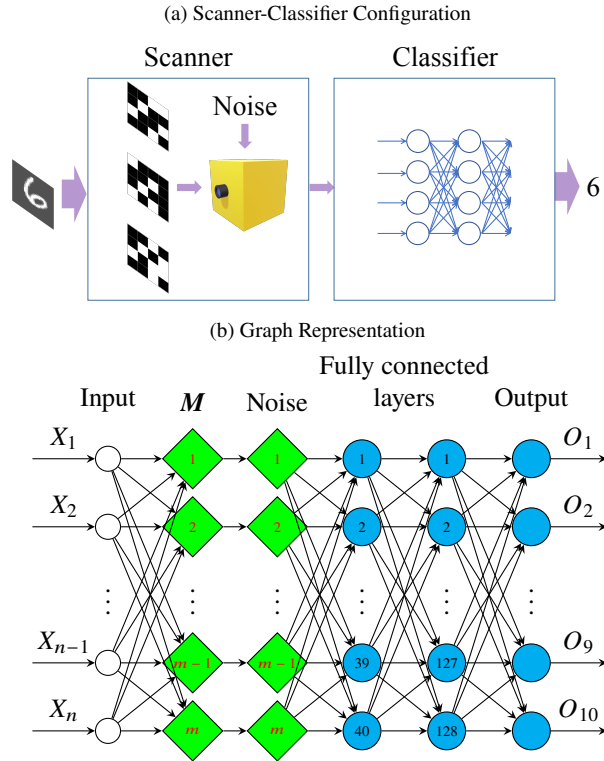


Fig. 2. (a) the general configuration of scanner-classifier networks. (b) the node-level architecture of our scanner (green diamonds)-classifier (blue circles) network. Noise is implemented after the sensing matrix  $M$ . Different from other coding schemes, DeepFSI has a trainable scanner where  $M$  is not fixed and can be optimized by the gradient of the classifier.

To further prove the necessity of our hardware optimization methodology and its versatility across a wide range of modern computer vision tasks beyond MNIST, we use the same scanner model with a Vision Transformer (ViT) as the classifier. The ViT model is adjusted to work with CIFAR10 data resized to 64 by 64 pixels. To better simulate a real computer vision system, we use only grayscale images with smaller 8-by-8 patch sizes following the classical FSI configuration [8], without any image enhancements or other preprocessing steps. The overall architecture is shown in Fig. 3. This model is referred to as the Optical-frontend Vision Transformer (OViT) in this context, and it serves as another DeepFSI example.

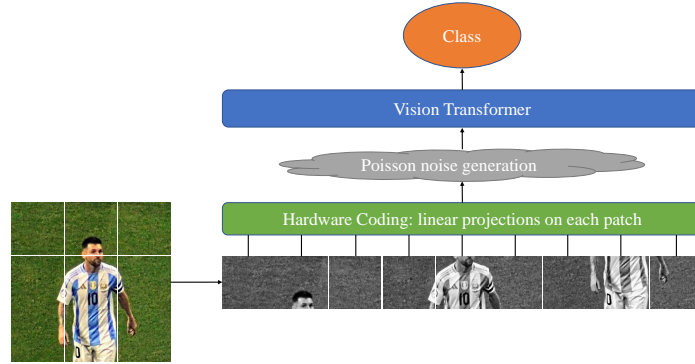


Fig. 3. OViT Overview. The process begins by dividing the input image into fixed-size grayscale patches. Poisson noise is then added after the initial linear projection to mimic optical coding within a vision system. These noisy embeddings are subsequently fed into a Vision Transformer.

#### 4.2. Simulated Experiments Design

In this section, we present two distinct classification tasks. Initially, we evaluated the effectiveness of various coding schemes using the MNIST dataset, focusing on their performance in number recognition. Subsequently, we extend the evaluation to CIFAR10 by OViT, examining the adaptability and efficacy of DeepFSI in this different domain.

The MNIST dataset, which consists of handwritten digits ranging from 0 to 9, has a default size of 28 by 28 pixels [36]. To align the data with Hadamard matrices, we add black pixels to the edges of the images and resize them to 32 by 32 pixels [36]. Subsequently, we rescale the pixel values from the original range of  $[0, 1]$  to  $[0.3, 1]$ . This rescaling introduces non-zero Poisson noise to the black regions, which has variance proportional to the expected photon counts.

We evaluate our proposed model through simulations under both AGN and Poisson noise models, using varying number of photons sent to the system to generate results at different noise levels. We also test all compressible strategies (TH, FSI, DeepFSI), varying the total number of masks  $m$  for a given number of photons, and define a metric called the compression ratio as the ratio of the number of masks to the number of pixels, i.e.  $m/N$  [37]. For II, RS and HB, this ratio is restricted to 1.00, while the rest, TH, FSI, DeepFSI, are evaluated over values in  $\{1\%, 4\%, 9\%, 16\%, 25\%, 36\%, 49\%, 64\%, 81\%, 100\%\}$  so that  $\mathbf{M}$  of each coding scheme is not restricted to being full-rank. The final result for a certain number of photons and a certain compression ratio is the average of five independent trials. As we target on investigating the maximum feature fidelity of each coding design, the best performance among the compression list is selected for final comparison. We notice the initial  $\mathbf{M}$  for DeepFSI can affect performance in the presence of noise. We therefore initialized its  $\mathbf{M}$  with the PCA components from the training data for a direct comparison with FSI.

On top of the classification tasks on MNIST dataset, we also try to apply DeepFSI onto a Vision Transformer, i.e. OViT in this work, to show that this methodology can be applied on more challenging and complicated vision tasks, with modern computer vision models. The optimization of OViT is similar to the model used on MNIST classification. However, no coding designs are compressed under the assumption that we have no prior knowledge about the optimal compression ratio, which is also unavailable beforehand in most real-world projects. This work can serve as a good example that demonstrates the robustness of DeepFSI over traditional FSI, especially when the best compression ratio is unavailable or the test conditions are not similar

enough.

### 4.3. Hardware Experiments Design

A key concern with DeepFSI is that its optimization relies on simulation, and its feasibility in real-world vision systems remains to be experimentally validated. We are also interested in whether DeepFSI is more robust than FSI when the experimental conditions do not perfectly match those in simulation. Therefore, we deploy the methodology implemented for the MNIST in Section 4.2 on a lab SPC. As shown in Fig. 4, the experiment utilizes a DMD (digital micromirror device), specifically the DLP 7000 model from Texas Instruments, and a PMT (photomultiplier tube) from PicoQuant, specifically the PMA Series. The training stage is conducted on a computer, and the parameters are deployed on the SPC to recognize handwritten number pictures displayed on a monitor. The testset consisted of ten pictures and each handwritten number appeared exactly once.

Similar to OViT experiments introduced in Section. 4.2, the optimal compression ratio is not available. We decide to use 0.09 in this case as its overall performance in the simulation is satisfactory. In other word TH, FSI and DeepFSI use 92 masks, while others use 1024 masks. All tests are repeated for three times, and the final performance is the average of the three trials. For each coding design, we test its performance when the total exposure times are 0.001, 0.01, 0.1, and 1.0 seconds.

Fig. 4 shows the hardware setup in this work. The first crucial step is to transform the digital

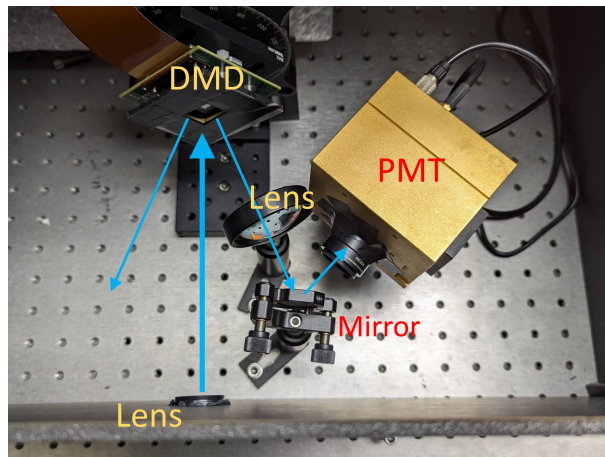


Fig. 4. Experimental configuration of the single-pixel camera: The light path is illustrated by the blue arrows in the diagram. Specifically, our setup utilizes only one branch reflected by the DMD.

MNIST data to ensure that they are consistent with the pictures on the monitors in the SPC’s perspective, as demonstrated in Fig. 5. The transformed MNIST is then used in DeepFSI training, and the optimized mask-set digitalized from  $\mathbf{M}$  is loaded onto the DMD. After the photon numbers are acquired, they are digitalized and vectorized and inputted to the classifier module on computer for number recognition.

The mask-set is not required to be binary in this work, though DMD only have ON and OFF states. Our approach is to select a random fraction of micromirrors in a pixel to achieve decimal real numbers. The DLP 7000 consists of  $1024 \times 768$  micromirrors, which project  $32 \times 32$  masks. Therefore, one pixel includes  $32 \times 24$  micromirrors. Using this method, we can achieve a precision of  $1.3 \times 10^{-3}$ , which is sufficient in this work. Fig. 6 shows an example of this trick.

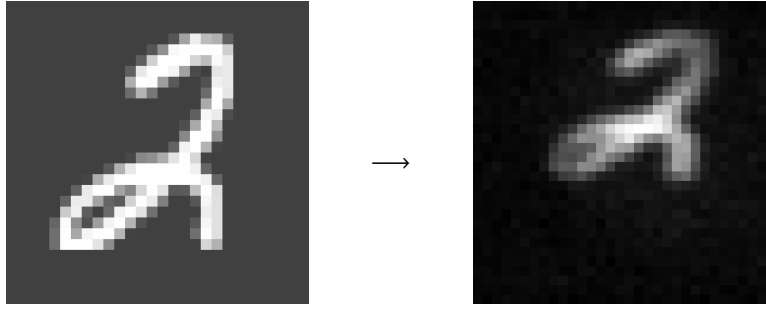


Fig. 5. Raw image (left) VS SPC-observed image

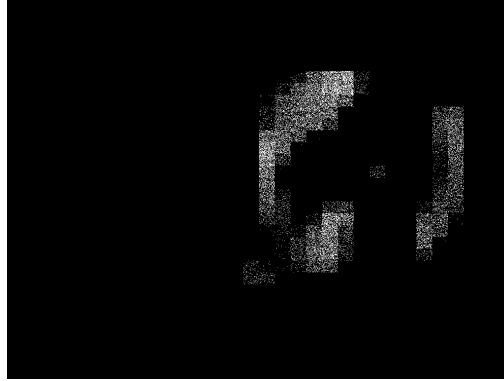


Fig. 6. A DMD mask with decimal values. Black regions are OFF-state and white regions are ON-state mirror chips. A coding pixel consists of  $32 \times 24$  mirror chips and the ratio of the white ones inside it represents the mask value at that pixel.

## 5. Results

### 5.1. Simulated Experiments on MNIST

Fig. 7 displays the classification performance of different coding schemes in the simulated experiments. Since PN is signal dependent and AGN is constant in this work, comparing the performance under both models is not straightforward if we simply use the total number of photons as x-coordinates. In this case, data points with the same x-coordinate are not affected by the same amount of noise when comparing across noise models. In other words, when provided with a certain number of photons, the variances caused by AGN and PN are not equal. However, the reconstruction error of  $\Pi$  is unique under an arbitrary photon number. Therefore, we choose a metric of the reconstruction error with  $\Pi$  to demonstrate the amount of noise regardless of its type and use it as the x-coordinate in the figure.  $\Pi$  is the gold standard, labeling the supreme among all the coding designs in this work. By this metric, we can compare feature fidelity among different coding designs even between AGN and PN as long as the x-coordinates are the same. As mentioned in Section 4.2, the simulations cover various compression ratios. To compare the maximum capacity of preserving features, we choose the best within different compression ratios for each coding design. If a coding design outperforms another in classification in Fig. 7, we can identify that it has better feature fidelity **if used optimally**. Feature-specific ones are indicated by circles, while non-feature-specific ones are marked by squares across both subfigures for clarity.

In Fig. 7a, we can identify that FSI and DeepFSI are much better than non-FSI coding designs. DeepFSI is also better than FSI and provides a performance most similar to that of the ideal  $\Pi$

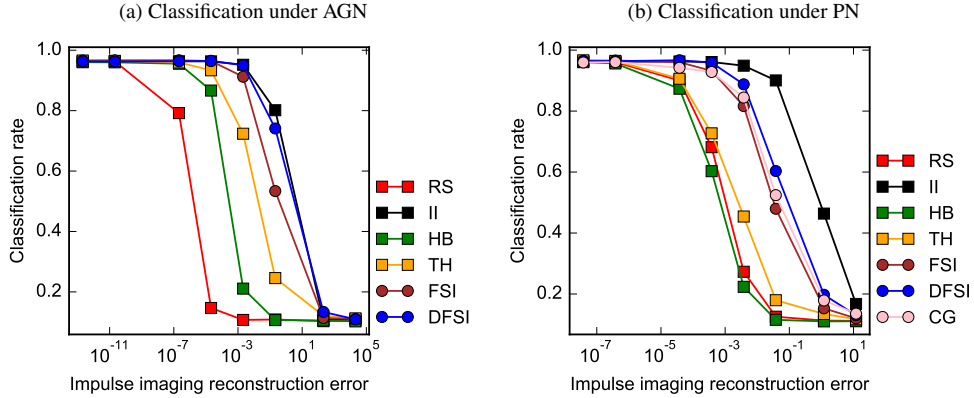


Fig. 7. Classification rates on **simulated data**. RS: Raster scan. HB: Hadamard basis. II: Impulse imaging. TH: Low Frequency Truncated Hadamard basis. FSI: PCA basis. DFSI: DeepFSI. CG: control group. Feature-specific methods are marked by  $\circ$  from traditional ones marked by  $\square$ . The CG employs the optimized masks under the AGN and trains the software classifier under PN. Its overall performance is still worse than DeepFSI.

camera. All basis scan methods, including HB and TH that are without prior information, are better than RS, which scans pixels in sequence. This result aligns with the common sense that coding can improve the performance under AGN.

In Fig. 7b, we see that PN degrades the performance of any coding designs, and using non-FSI coding cannot provide a performance gain compared to RS. FSI presents better performance than non-FSI methods, although it is not designed for PN, which is consistent with the discovery of Nahalanobis et al. [10]. It highlights the necessity of using data priors under PN in a vision system. More significantly, DeepFSI outperforms traditional FSI, showing the advantage of using end-to-end optimization compared to PCA under PN. Additionally, we present a control group that first optimizes the coding under AGN and subsequently optimizes the classifier with this coding fixed under PN. We observe a suboptimal performance on the control group, indicating that using the optimal coding under AGN cannot lead to optimal performance in a vision system. It is an important discovery that the crucial role of noise models for the regime of future camera design.

## 5.2. Robustness Analysis

We notice a shortcoming that may affect the practicality of traditional FSI that the optimal number of masks, or the row number in  $\mathbf{M}$ , is unknown before optimization. Furthermore, once  $\mathbf{M}$  is optimized, its performance under conditions different from those in the training stage may no longer be optimal. Therefore, we also design an experiment to test the robustness of TH, FSI and DeepFSI under PN. For each coding design, we keep using the compression ratios in Section 4.2, but fix the total number of photons at  $10^5$  in training stage. For each compression ratio, we test the optimized coding design with different photon numbers and show the classification rates in Fig. 8.

Focusing at the values when number of photon is  $10^5$ , we can see a tremendous performance degradation in FSI if we choose an improper number of masks, although its performance supreme is much better than that of non-FSI methods, i.e. the truncated hadamard in this example. However, while the overall performance is no worse than FSI, DeepFSI presents more robust

classification rates when the number of masks is suboptimal. Given that it is challenging to know the proper number of masks in real-world applications as it depends on the task and training data, DeepFSI has a significant feature of greater tolerance, which greatly improves the practicality compared to FSI.

Focusing at the values with the same compression ratio, we can see the all models' performances are robust when used in less noisy environments where numbers of photons are above  $10^5$  in this work, but dramatically drop when used in noisier environments. We can learn that we should optimize the models with more noise to ensure that their performances are robust in potential situations after setup in practice.

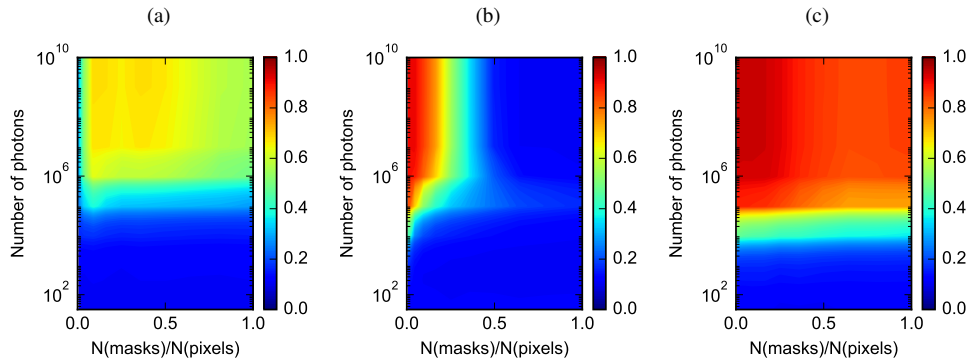


Fig. 8. Classification rates on simulated data regarding compression ratios and light levels with (a) Truncated Hadamard, (b) FSI, and (c) DeepFSI. The models are trained under Poisson noise using a light level of  $10^5$  photons and subsequently tested under different light levels. It is observed that FSI performance deteriorates when the compression ratio is not properly chosen, whereas the Truncated Hadamard and DeepFSI models exhibit greater robustness in such scenarios.

### 5.3. *OViT Simulations*

Fig. 9 shows the classification rates on the CIFAR10 dataset with PN, based on simulation results. In this experiment, we assume the best compression rate is unavailable, and all coding designs employs  $m = N$  masks where  $N$  is the number of pixels in a patch. When PN is present, OViT outperforms all non-FSI coding strategies. This result shows DeepFSI's feasibility in more complicated vision tasks, and verifies its robustness with wrong compression ratio in Section 5.2, suggesting DeepFSI is a more practical method than FSI in general. Notably, our optical scanner module is simply a fully connected layer, much smaller in size compared to the ViT classifier. This further underscores that any software cannot ever fully compensate for the performance limitations of suboptimal hardware. This supports our perspective that once data are measured with suboptimal coding in any vision system, its overall performances on subsequent computer vision tasks are strictly bounded. All modern computer vision algorithms, unless they also optimize the hardware, are constrained by the upper bound set by the hardware and cannot exceed it, preventing them from fully exploiting their true performance potential.

### 5.4. *Hardware Experiments on MNIST*

Fig. 10 compares the classification rates of different coding designs in a hardware experiment. We see that DeepFSI outperforms the other coding by a huge margin. This phenomenon can be explained by the results in Section. 5.2 that DeepFSI provides better tolerance and performance

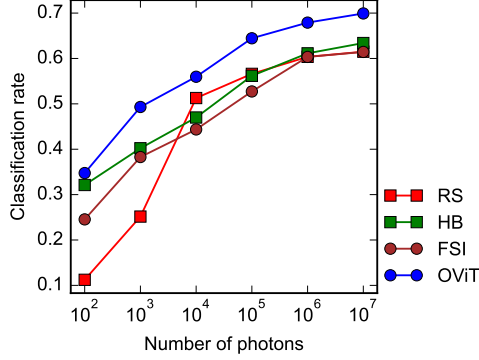


Fig. 9. Classification rates of different optical coding with ViT on CIFAR10 under Poisson noise. RS: Raster basis. HB: Hadamard basis. FSI: PCA basis. OViT: Optical-frontend Vision Transformer. The x-axis indicates the total number of photons used in the corresponding simulation.

than the other coding designs when the compression ratio used is not ideal or not available, which is fixed at 0.09 in this experiment. In real-world applications, noise can be more complex than what is considered in this work. Factors such as ambient light and dark counts can cause the vision system to deviate from its supreme achieved in training conditions, leading to unexpected performance degradation to other coding designs shown in Fig. 10. Therefore, the robustness and tolerance of DeepFSI are of great value in the promotion of task-specific imaging.

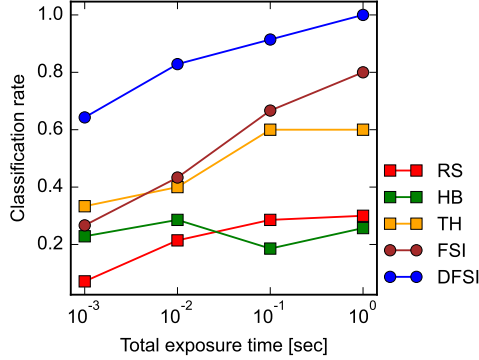


Fig. 10. Classification rates of different optical coding on MNIST in the hardware experiment. RS: Raster basis. HB: Hadamard basis. TH: truncated Hadamard basis. FSI: PCA basis. DFSI: DeepFSI. The x-axis represents the total exposure time.

## 6. Discussion and Limitations

We propose a deep feature-specific imaging model to complement conventional feature-specific imaging techniques, which is originally designed for additive Gaussian noise, under Poisson noise. Its performances have been tested with a single-pixel camera compared to other coding designs. DeepFSI presents a better performance than that of FSI under Poisson noise and a better practicality and tolerance in real-world implementation as well. Since Poisson noise is a growing challenge for photon-counting technology in future vision systems design, the proposed model extended the applicability of sensors using such technology.

In addition to some facts already known to many, such as that a higher light throughput may not guarantee a better performance which is shown in Fig. 7, this work also discloses several other interesting phenomena. First, using AGN-optimal coding under PN is not recommended as the computed gradient on optical coding layer in these two models are different, indicating different directions during optimization. Second, future camera or vision system design must incorporate hardware optimization to achieve the best performance. However, this end-to-end optimization must be performed under the correct noise model.

One limitation in this work is that we use the MLGauss noise model whose variance and mean are equal and apply reparameterization to approximate the actual photon noise at the sensor during training. This approach offers a valid alternative to Poisson noise in gradient estimation when the number of photons is greater than 10 [13], but it may not provide the same performance gain at extremely low-light conditions, where the actual Poisson noise for testing deviates more from it. A potential future direction is to develop a more accurate reparameterization model tailored for such low-light scenarios.

## 7. Back matter

**Funding.** This work is supported by the National Science Foundation (1846884) and the Air Force Office for Scientific Research (FA9550-21-1-0341).

## References

1. A. Ingle, A. Velten, and M. Gupta, "High flux passive imaging with single-photon sensors," in *Proceedings of the IEEE/CVF Conference on Computer Vision and Pattern Recognition*, (2019), pp. 6760–6769.
2. T. Niehörster, A. Löschberger, I. Gregor, *et al.*, "Multi-target spectrally resolved fluorescence lifetime imaging microscopy," *Nat. methods* **13**, 257–262 (2016).
3. I. M. Antolovic, S. Burri, C. Bruschini, *et al.*, "Spad imagers for super resolution localization microscopy enable analysis of fast fluorophore blinking," *Sci. reports* **7**, 44108 (2017).
4. Y. Altmann, S. McLaughlin, M. J. Padgett, *et al.*, "Quantum-inspired computational imaging," *Science* **361**, eaat2298 (2018).
5. O. Cossairt, M. Gupta, and S. K. Nayar, "When does computational imaging improve performance?" *IEEE transactions on image processing* **22**, 447–458 (2012).
6. M. Raginsky, R. M. Willett, Z. T. Harmany, and R. F. Marcia, "Compressed sensing performance bounds under poisson noise," *IEEE Trans. on Signal Process.* **58**, 3990–4002 (2010).
7. M. Harwit and N. J. A. Sloane, *Hadamard Transform Optics* (Academic Press, 1979).
8. M. Neifeld and P. Shankar, "Feature-specific imaging," *Appl. optics* **42**, 3379–89 (2003).
9. H. S. Pal and M. A. Neifeld, "Multispectral principal component imaging," *Opt Express* **11**, 2118–25 (2003 Sep 8).
10. A. Mahalanobis and M. Neifeld, "Optimizing measurements for feature-specific compressive sensing," *Appl. Opt.* **53**, 6108–6118 (2014).
11. P. K. Baheti and M. A. Neifeld, "Adaptive feature-specific imaging: a face recognition example," *Appl. optics* **47**, B21–B31 (2008).
12. A. Wuttig, "Optimal transformations for optical multiplex measurements in the presence of photon noise," *Appl. Opt.* **44**, 2710–2719 (2005).
13. K. Mitra, O. Cossairt, and A. Veeraraghavan, "Can we beat hadamard multiplexing? data driven design and analysis for computational imaging systems," in *2014 IEEE International Conference on Computational Photography (ICCP)*, (IEEE, 2014), pp. 1–9.
14. N. Ratner, Y. Y. Schechner, and F. Goldberg, "Optimal multiplexed sensing: bounds, conditions and a graph theory link," *Opt. express* **15**, 17072–17092 (2007).
15. M. Mordechay and Y. Y. Schechner, "Matrix optimization for poisson compressed sensing," in *2014 IEEE Global Conference on Signal and Information Processing (GlobalSIP)*, (IEEE, 2014), pp. 684–688.
16. S. Diamond, V. Sitzmann, F. Julca-Aguilar, *et al.*, "Dirty pixels: Towards end-to-end image processing and perception," *ACM Trans. on Graph. (TOG)* **40**, 1–15 (2021).
17. K. Zhang, J. Hu, and W. Yang, "Deep compressed imaging via optimized pattern scanning," *Photonics research* **9**, B57–B70 (2021).
18. R. Jacome, P. Gomez, and H. Arguello, "Middle output regularized end-to-end optimization for computational imaging," *Optica* **10**, 1421–1431 (2023).
19. T. Klinghoffer, S. Somasundaram, K. Tiwary, and R. Raskar, "Physics vs. learned priors: Rethinking camera and algorithm design for task-specific imaging," in *2022 IEEE International Conference on Computational Photography (ICCP)*, (IEEE, 2022), pp. 1–12.
20. J. Chang, V. Sitzmann, X. Dun, *et al.*, "Hybrid optical-electronic convolutional neural networks with optimized diffractive optics for image classification," *Sci. reports* **8**, 1–10 (2018).
21. C. Hinojosa, J. C. Niebles, and H. Arguello, "Learning privacy-preserving optics for human pose estimation," in *Proceedings of the IEEE/CVF international conference on computer vision*, (2021), pp. 2573–2582.
22. X. Dun, H. Ikoma, G. Wetzstein, *et al.*, "Learned rotationally symmetric diffractive achromat for full-spectrum computational imaging," *Optica* **7**, 913–922 (2020).
23. C. A. Metzler, H. Ikoma, Y. Peng, and G. Wetzstein, "Deep optics for single-shot high-dynamic-range imaging," in *Proceedings of the IEEE/CVF Conference on Computer Vision and Pattern Recognition*, (2020), pp. 1375–1385.
24. J. Chang and G. Wetzstein, "Deep optics for monocular depth estimation and 3d object detection," in *Proceedings of the IEEE/CVF International Conference on Computer Vision*, (2019), pp. 10193–10202.
25. E. Onzon, F. Mannan, and F. Heide, "Neural auto-exposure for high-dynamic range object detection," in *Proceedings of the IEEE/CVF conference on computer vision and pattern recognition*, (2021), pp. 7710–7720.
26. J. Spall, X. Guo, and A. I. Lvovsky, "Hybrid training of optical neural networks," *Optica* **9**, 803–811 (2022).
27. G. M. Gibson, S. D. Johnson, and M. J. Padgett, "Single-pixel imaging 12 years on: a review," *Opt. express* **28**, 28190–28208 (2020).
28. J. D. Rego, H. Chen, S. Li, *et al.*, "Deep camera obscura: an image restoration pipeline for pinhole photography," *Opt. Express* **30**, 27214–27235 (2022).
29. M. F. Duarte, M. A. Davenport, D. Takhar, *et al.*, "Single-pixel imaging via compressive sampling," *IEEE Signal Process. Mag.* **25**, 83–91 (2008).

30. T. Wang, S.-Y. Ma, L. G. Wright, *et al.*, “An optical neural network using less than 1 photon per multiplication,” *Nat. Commun.* **13**, 123 (2022).
31. Y. Xu, W. Liu, and K. F. Kelly, “Compressed domain image classification using a dynamic-rate neural network,” *IEEE Access* **8**, 217711–217722 (2020).
32. E. Tseng, A. Mosleh, F. Mannan, *et al.*, “Differentiable compound optics and processing pipeline optimization for end-to-end camera design,” *ACM Trans. on Graph. (TOG)* **40**, 1–19 (2021).
33. R. Raskar, “Computational photography: Epsilon to coded photography,” in *Emerging Trends in Visual Computing: LIX Fall Colloquium, ETVC 2008, Palaiseau, France, November 18-20, 2008. Revised Invited Papers*, (Springer, 2009), pp. 238–253.
34. A. K. Boyat and B. K. Joshi, “A review paper: Noise models in digital image processing,” *ArXiv* **abs/1505.03489** (2015).
35. M. Selwood, “Coded aperture imaging: novel approaches to high-energy high-resolution laboratory imaging,” Ph.D. thesis, University of York (2022).
36. Y. Lecun, L. Bottou, Y. Bengio, and P. Haffner, “Gradient-based learning applied to document recognition,” *Proc. IEEE* **86**, 2278–2324 (1998).
37. R. Stojek, A. Pastuszczak, P. Wróbel, and R. Kotyński, “Single pixel imaging at high pixel resolutions,” *Opt. Express* **30**, 22730–22745 (2022).